Tectonophysics 746 (2018) 312–324

Contents lists available at ScienceDirect

Tectonophysics

journal homepage: www.elsevier.com/locate/tecto

The role of deep subduction in supercontinent breakup

Luca Dal Zilio [a,*], Manuele Faccenda [b], Fabio Capitanio [c]

[a] Institute of Geophysics, ETH Zurich, 8092 Zurich, Switzerland
[b] Department of Geosciences, Università degli Studi di Padova, via G. Gradenigo, 6, 35131 Padova, Italy
[c] School of Earth, Atmosphere and Environment, Monash University, Clayton, Victoria 3800, Australia

ARTICLE INFO

Article history:
Received 14 September 2016
Received in revised form 1 March 2017
Accepted 8 March 2017
Available online 10 March 2017

Keywords:
Subduction
Supercontinent breakup
Plate tectonics
Geodynamic
Subduction-induced mantle flow
Numerical modeling

ABSTRACT

The breakup of continents and their subsequent drifting plays a crucial role in the Earth's periodic plate aggregation and dispersal cycles. While continental aggregation is considered the result of oceanic closure during subduction, what drives sustained divergence in the following stages remains poorly understood. In this study, thermo-mechanical numerical experiments illustrate the single contribution of subduction and coupled mantle flow to the rifting and drifting of continents. We quantify the drag exerted by subduction-induced mantle flow along the basal surface of continental plates, comparing models of lithospheric slab stagnation above the upper-lower mantle boundary with those where slabs penetrate into the lower mantle. When subduction is upper-mantle confined, divergent basal tractions localise at distances comparable to the effective upper mantle thickness (~500 km), causing the opening of a marginal basin. Instead, subduction of lithosphere in the lower mantle reorganises the flow into a much wider cell localising extensional stresses at greater distances from the trench (~3000 km). Sub-continental tractions are higher and more sustained over longer time periods in this case, and progressively increase as the slab sinks deeper. Although relatively low, basal-shear stresses when integrated over large plates, generate tension forces that may exceed the strength of the continental lithosphere, eventually leading to breakup and opening of a distal basin. The models illustrate the emergence of a similar mechanism, which results in the formation of back-arc basins above upper-mantle confined subduction, and scales to much larger distances for deeper subduction. Examples include the Atlantic Ocean formation and drifting of the South and North American plates during the Mesozoic-Cenozoic Farallon plate subduction.

1. Introduction

The mechanism of rifts and breakup in continent interiors remains to date an open question in plate tectonics. For example, in the Mesozoic, large-scale rifting deformed the interior of Pangea, culminating in its complete dismemberment when the North and South American plates drifted away from Europe and Africa, opening the Atlantic Ocean (Wilson, 1966). Rifting was likely sustained for a long time before breakup, and the overall divergence along this margin lasted until the Cenozoic. Although this is a key stage of the aggregation-dispersal of the tectonics cycle, why large continents rift in their interiors and eventually breakup remains an unsolved issue in plate tectonics theory.

Given the established relation between the present-day mantle structure and plate tectonic evolution in the last 120 Ma (Bunge et al., 1998), it is expected that supercontinent assembly and breakup processes would be associated with mantle dynamics and structure. In the last 30 years, mantle convection and its convective wavelength have been extensively studied in dynamically self-consistent three-dimensional spherical shell mantle convection models (e.g., Tackley et al., 1993; Yoshida, 2014; Zhong and Gurnis, 1993; Zhong et al., 2007). These models have revealed that the most important controlling parameter on convective wavelength is the mantle viscosity structure (e.g., Lenardic et al., 2006), Rayleigh number (*Ra*), solid-solid phase changes (Tackley et al., 1993), and mantle compressibility (e.g., Zhong and Liu, 2016, and references therein). However, the temporal evolution of the convective wavelength remains an intriguing question, particularly because it has important implications for the location of major mantle upwellings and the initiation of continental breakup. While the present-day Earth's mantle structure is dominantly at spherical harmonic degree-2 (Zhong et al., 2007), how mantle structure may have evolved in the geological past is still unclear. Once Pangea was formed, the circum-supercontinent subduction would lead to upwellings and thermal insulation beneath the supercontinent, thus changing the degree-1 mantle structure to degree-2 with two major antipodal upwellings, similar to the present-day Earth's mantle (Zhong et al., 2007). The hot upwellings beneath the supercontinent would cause magmatism and eventual breakup of the supercontinent. However, Burov and Gerya

* Corresponding author.
E-mail address: luca.dalzilio@erdw.ethz.ch (L. Dal Zilio).

http://dx.doi.org/10.1016/j.tecto.2017.03.006
0040-1951/

(2014) and Koptev et al. (2015) recently showed that axi-symmetric mantle upwellings cannot cause rifting by themselves, although they contribute by localising the deformation from far-field extensional tectonic forces that are strictly required to generate the breakup of structurally homogeneous continents.

Where do these far-field extensional stresses come from? Subduction and subsequent roll-back of oceanic plates at continental margins have been invoked to support the occurrence of large-scale, long-term extensional stresses, thus leading to supercontinental dispersal (e.g., Bercovici and Long, 2014; Lowman and Jarvis, 1996). Moreover, numerical models show that downgoing slabs play a central role in establishing the location and formation of subcontinental mantle plumes via mass conservation (Tan et al., 2002; Heron and Lowman, 2011; Heron et al., 2015; Lenardic et al., 2011; Zhang et al., 2010; Zhong et al., 2007). If this is indeed the main factor that drives heating below a supercontinent, this suggests that the mantle beneath Pangea would experience a significant increase in temperature, which may be responsible for its breakup (Lenardic et al., 2011).

Several of the proposed mechanisms of large-scale mantle flow indicate that the interaction between subducting slabs and supercontinents dispersal might be of relevance, although a more systematic understanding of role of the subduction process in isolation, and the induced mantle flow and breakup of large continents, remains elusive. Subduction-induced mantle flow can generate shear stresses along the base of the lithosphere beneath continental plates (Melosh, 1977). In a subduction setting, basal drag and suction forces due to slab roll-back are commonly invoked as causes of the opening of back-arc basins, such as the Japan Sea (Jolivet et al., 1994) and the Western Mediterranean (Faccenna et al., 2001) (Fig. 1). These back-arc basins, also known as marginal basins, are consistently located 250–500 km away from the trench, where the continent has rifted and eventually drifted away leaving oceanic floor in its wake. Back-arc basins also show relationships between subduction and anomalous volcanism, which seems to be related to the subduction-related return flow. In several regions, there is evidence for volcanism spatially and temporally connected to subduction zones. Relationships between subduction and anomalous volcanism, already postulated to explain regional cases of intraplate magmatic activity (e.g., Zhao, 2004; Zhao et al., 2009), have also been investigated numerically (Garfunkel et al., 1986; Faccenna et al., 2010). Results showed how the 660-km viscosity jump and trench roll-back can influence the return flow in the upper mantle. Similar characteristics of rifting-drifting episodes and subsequent oceanization are reconstructed in the Mesozoic dismembering of Pangea. However, rifting occurred here at 2000–5000 km from the reconstructed Farallon subduction trench, extended along-strike for >10.000 km, and lasted for more than ~130 Ma (Seton et al., 2012), which is indicative of a rather similar, although larger-scale and long-lived, process.

In this paper, we analyse the contribution of a single, spontaneous subduction process on supercontinent breakup, using a similar approach to authors such as Běhounková and Čížková (2008) and Holt et al. (2015). We focused the study on the effects of subduction dynamics and related mantle flow on continental breakup. Our intent is to (1) identify how slab dynamic end-members (i.e. stagnating in the mid-mantle vs. penetrating deeper into the lower mantle) can affect the breakup mechanism and location; (2) characterize the breakup mechanism responsible for each subduction end-member, quantifying the acting forces; (3) investigate how the mantle flow induced by subduction evolves through time; (4) quantify the basal drag development beneath a supercontinent subjected to mantle flow and (5) evaluate for which continental strengths breakup may occur.

2. Numerical modeling method

2.1. Governing equations and method

Numerical experiments were carried out with I2VIS (Gerya and Yuen, 2003), a numerical framework which solves the continuity, momentum and heat conservation equations for a 2D creeping flow. Conservation of mass is approximated by the continuity-compatibility equation:

$$\frac{\partial \rho}{\partial t} + \nabla\left(\rho \vec{v}\right) = 0, \tag{1}$$

where ρ is local density and $\vec{v}$ is the local velocity vector. In our models the material is assumed to be compressible (i.e. density of material

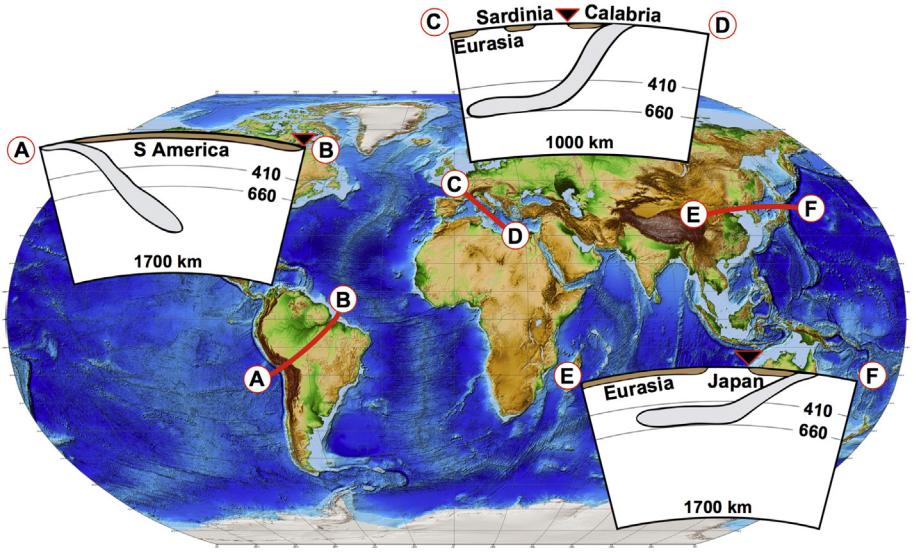

Fig. 1. World topographic map and schematic cross sections of subduction zones extrapolated from P-wave tomographic models. Solid triangles show rifted continental margins and the 410 and 660 km discontinuities are indicated as thin grey lines. The grey bodies are fast velocity anomalies, interpreted as subducting slabs, while the brown bodies at the surface represent continental plates. A–B) Cross section across the South American plate (Li et al., 2008), with subduction of the Nazca plate beneath the South American plate and its penetration into the lower mantle to a depth > 1200 km. C–D) Cross section of the central Mediterranean region (Piromallo and Morelli, 2003), with the Ionian slab subducting beneath Calabria and stagnating over the 660 km discontinuity. A similar case can be found on the east–west cross section E–F through the Japan arc (Fukao et al., 2009), where the Pacific plate stagnates in the transition zone. Note that both in the Calabria and Japan arcs, subducting plates are coupled with microcontinents, while subduction along the western margin of the South American plate is coupled with a large continent.

points may change with time). Hence, the 2D continuity equation takes the form:

$$\frac{\partial v_x}{\partial x}+\frac{\partial v_y}{\partial y}=-\frac{1}{\rho}\ \frac{D\rho}{Dt} \tag{2}$$

where $D\rho/Dt$ is the substantive density time derivative, v_x and v_y are, respectively, the horizontal and vertical velocity component, x and y denote horizontal and vertical Cartesian coordinates. The momentum equations are presented in the form of the Stokes flow approximation:

$$\frac{\partial \sigma'_{ij}}{\partial x_j}-\frac{\partial P}{\partial x_i}+\rho g_i=0 \tag{3}$$

which in 2D reads:

$$\frac{\partial \sigma'_{xx}}{\partial x}+\frac{\partial \sigma'_{xy}}{\partial y}-\frac{\partial P}{\partial x}=0 \tag{4.1}$$

$$\frac{\partial \sigma'_{yy}}{\partial y}+\frac{\partial \sigma'_{yx}}{\partial x}-\frac{\partial P}{\partial y}=-\rho g_y \tag{4.2}$$

where P is the pressure, σ'_{ij} are the components of the viscous deviatoric stress tensor, ρ is the density dependent on rock composition, temperature and pressure, and $\vec{g}$ is the acceleration due to gravity. The components of the deviatoric stress tensor (σ'_{ij}) are calculated using the viscous constitutive relationship between stress and strain rate ($\dot{\varepsilon}$), as follows:

$$\sigma'_{ij}=2\eta\dot{\varepsilon}'_{ij}=2\eta(\dot{\varepsilon}_{ij}-1/3\delta_{ij}\dot{\varepsilon}_{kk}) \tag{5}$$

$$\dot{\varepsilon}_{ij}=\frac{1}{2}\left(\frac{dv_i}{dx_j}+\frac{dv_j}{dx_i}\right) \tag{6}$$

The conservation of energy equation describes the temperature changes in a continuum due to internal heat generation/consumption and advective/conductive heat transport. The balance of heat in 2D is:

$$\rho c_{P\_eff}\left(\frac{\partial T}{\partial t}+v\ grad(T)\right)=-\frac{\partial q_x}{\partial x}-\frac{\partial q_y}{\partial y}+H_r+H_a+H_s, \tag{7}$$

where q_x and q_y are heat flux components; $k=f(P,T,C)$ is thermal conductivity which depends on the pressure-temperature conditions and composition. H_r, H_a and H_s are, respectively, radioactive, adiabatic and shear heat production. Radioactive heat production depends on the rock type and it is assumed to be constant through time. The adiabatic heat production/consumption is related to pressure changes (compression-decompression):

$$H_a=T\alpha_{eff}\left(v_x\frac{\partial P}{\partial x}+v_y\frac{\partial P}{\partial y}\right). \tag{8}$$

The shear heat production is given by the dissipation of mechanical energy during viscous deformation and depends on the deviatoric stress and deviatoric strain rate:

$$H_s=\sigma'_{xx}\dot{\varepsilon}'_{xx}+\sigma'_{yy}\dot{\varepsilon}'_{yy}+2{\cdot}\sigma'_{xy}\dot{\varepsilon}'_{xy}. \tag{9}$$

The effect of latent heating related to the phase transformations of the rocks is included implicitly by calculating the effective heat capacity (c_{P_eff}) and the effective thermal expansion (α_{eff}) through thermodynamic relations, as in Gerya (2010). Petrological phase changes are implemented using a thermodynamic formulation for density, $\rho=f(P,T)$, and enthalpy, $Q=f(P,T)$ obtained from optimization of Gibbs' free energy for a typical mineralogical composition of mantle and crustal materials by using PERPLE_X (Connolly, 2005).

The visco-plastic behaviour is implemented via evaluation of the effective viscosity of the material. The viscous properties are computed by taking into account the contribution of different creep mechanisms such as diffusion, dislocation and Peierls creep, as:

$$\frac{1}{\eta_{eff}}=\frac{1}{\eta_{diff}}+\frac{1}{\eta_{disl}}+\frac{1}{\eta_{peierls}}, \tag{10}$$

where η_{diff}, η_{disl} and $\eta_{peierls}$ are calculated from flow laws defined in Ranalli (1995) and Katayama and Karato (2008). The strength of the material is limited by:

$$\eta_{eff}=\frac{\sigma_{yield}}{2\dot{\varepsilon}_{II}}, \tag{11}$$

where the yield stress is described at shallow depths by the Drucker-Prager yield criterion:

$$\sigma_{yield}=cos\phi{\cdot}C+sin\phi{\cdot}P(1-\lambda_{fluid}), \tag{12}$$

and at larger depths by the von Mises yield criterion

$$|\sigma_{yield}|=const, \tag{13}$$

Here, ϕ is the internal friction angle, C is the cohesion, and λ_{fluid} is the pore fluid pressure factor.

2.2. Model setup

The computational domain size is 15,000 × 3000 km and is discretised with 751 × 342 Eulerian nodes, with >8 million randomly distributed Lagrangian particles (Fig. 2). The model uses a regular grid spacing of 20 km in the horizontal direction and a variable grid spacing in the vertical direction: 2 km in the range of 0 to 40 km, 5 km from 40 to 90 km and 10 km below 90 km. By reducing to 10 km the horizontal grid spacing (Fig. S6) the subduction-induced mantle flow does not vary substantially with respect to the case with 20 km horizontal resolution (Fig. S1), which allows us to use the coarser grid. Free slip is imposed at the top boundary, while the left and right boundaries are periodic. No slip is imposed at the bottom boundary in order to define a Dirichlet boundary condition for the horizontal velocity component v_x, which is required in the finite difference method to invert the left-hand-side matrix. As the mantle is bounded by air and the liquid outer core, pseudo-free surface conditions at the top and bottom of the mantle are simulated by adding two low-viscosity layers: a 25 km thick, low-density air layer at the top that yields a more realistic one-sided subduction (Gerya et al., 2008); a 200 km thick, high-density layer at the bottom that ensures deep lower mantle flow past the outer core with negligible loss of energy due to viscous friction. Due to the adopted resolution, the oceanic plate is layered in a 20-km-thick crust and a 70-km-thick lithospheric mantle. The crust in the continental plate is instead 32-km-thick, while the thickness of the lithospheric mantle is varied from 44 to 118 km (Table 1). A half-space cooling model defines the 70 Ma geotherm within both plates (Fig. 2c, d, e), below which an adiabatic gradient of 0.5 K/km is imposed. In addition, for some specific cases a 150 Ma geotherm is used, yielding a 150 km thick continental plate in order to simulate a stiff cratonic keel. Buoyancy and strength of each compositional phase are related to the thermal structure through, respectively, a thermodynamic database of mantle densities (see below) and the visco-plastic rheological model (Fig. 2d, e). Subduction starts dynamically due to the negative buoyancy provided by a 200 km long cold slab.

In order to obtain realistic slab sinking scenarios, we have set the upper mantle viscosity to a reference value of $3\cdot10^{20}$ Pa s (e.g., Čížková et al., 2012; Mitrovica and Forte, 2004), and progressively increased that of the lower mantle to generate different viscosity contrasts between upper and lower mantle ($\boldsymbol{\gamma=\eta_{LM}/\eta_{UM}}$). Additionally, we

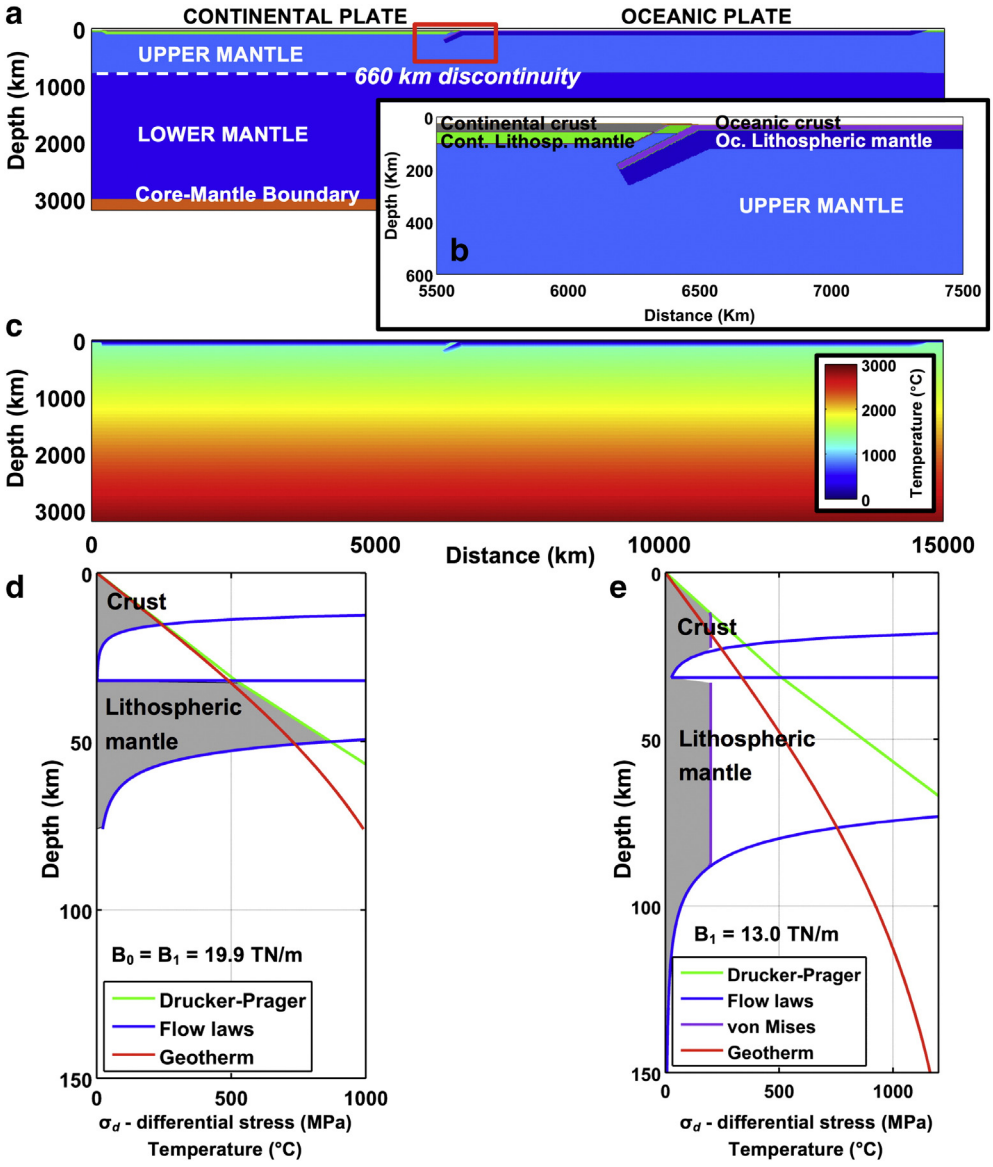

Fig. 2. Numerical setup of the reference model. (a) Numerical model setup characterized by the incipient subduction of an oceanic plate beneath a large continental plate. Panel (b) shows in detail the initial geometry around the oceanic trench. (c) Initial temperature distribution. Yield envelope profiles of the continental plate subjected to extensional deformation ($\dot{\varepsilon} = 10$–$14\ s^{-1}$) in (d) the reference model Test 118 (76 km thick and 70 Ma old lithosphere), and (e) the model with a cratonic root Test 168 (150 km thick, and 150 old lithosphere). See also Tables 1 and 2. Red curves are the initial geotherms calculated with the half-space cooling model. The initial and/or final integrated tensile strength (***B***) of the continental plates is given by the area of the regions in grey.

have tested a range of different viscosity profiles to test the role of a low-viscosity channel ($3 \cdot 10^{17} - 3 \cdot 10^{19}$ Pa s, Doglioni et al., 2011) in the 90–200 km depth range to simulate a weaker asthenosphere, non-Newtonian stress-dependent upper mantle (e.g., Gerya and Meilick, 2011), and temperature- and pressure-dependent profiles (e.g., Christensen, 1996) (Fig. 3).

We completed a broad spectrum of numerical experiments and systematically varied model parameters, such as upper-lower mantle viscosity contrast, mantle viscosity profiles, age of the subducting plate, and thickness and strength of the continental plate. Using different rheological parameters, listed in Tables 1 and 2, different regimes of subduction were reproduced in order to induce slab stagnation above the 660 km discontinuity or penetration into the lower mantle depending on (i) the upper–lower mantle viscosity contrast ($\boldsymbol{\gamma}$) (e.g., Christensen, 1996; Garel et al., 2014), and (ii) the oceanic slab age (e.g., King et al., 2015), in agreement with these authors. Using all these models which reproduce the range of published results, we measure the magnitude and time-evolution of mantle tractions by integrating shear stresses at the base of the overriding plate. These shear stresses are proportional to the upper mantle viscosity and to the velocity gradient along the vertical direction:

$$\sigma_{xy} \approx \eta \frac{\partial v_x}{\partial y} \tag{14}$$

Hence, a fast and viscous upper mantle flowing beneath a relatively stable plate produces high tractions. Trench-ward ($\boldsymbol{F_{TD}}$) and continent-ward ($\boldsymbol{F_{CD}}$) mantle drag were quantified by integrating the shear stress along the base of the continental plate as:

$$\boldsymbol{F_{CD}} = \int_A^B \sigma_{xy} \partial x, \tag{15.1}$$

$$\boldsymbol{F_{TD}} = \int_B^C \sigma_{xy} \partial x, \tag{15.2}$$

where *A*–*B* and *B*—*C* delimit the plate segments in which $\boldsymbol{F_{TD}}$ or $\boldsymbol{F_{CD}}$ act (Fig. S1). In our models, $\boldsymbol{F_{TD}}$ is due to the subduction-induced mantle

Table 1
Thermomechanical parameters used in these experiments. Set of parameters used for the model units, as follow: lithospheric thickness, constant density (ρ_0), pore fluid pressure factor (λ), von Mises yield criterion (σ_{yield}), age of the plates, radiogenic heat production (H_r), activation energy (E), stress exponent (n), activation volume (V), pre-exponential factor (A_d), cohesion (C), initial and final friction coefficient (μ_0,μ_1) and the corresponding strain values (ε_0,ε_1) within which μ linearly decreases due to strain weakening, and finally the reference flow law for dislocation creep taken from (Ranalli, 1995). A constant viscosity Ad was set when no rheological parameters are indicated. A dry olivine flow law was used for the upper mantle in Test 061.

Material	Thickness [km]	ρ_0 [kg/m^3]	λ_{fluid},–	σ_{yield} [MPa]	age [Myr]	H_r [Wm^{-3}]	E [kJ/mol]	n, –	V [J/(bar)]	A_D [Pa s]	C [MPa]	μ_0,μ_1	ε_0,ε_1	Flow law
Air	25	1								$1.0 \cdot 10^{18}$				
Water	5	1000								$1.0 \cdot 10^{18}$				
Background crust	30		0			$2.5 \cdot 10^{-7}$	154	2.3	1.2	$1.97 \cdot 10^{17}$	1	0.2, 0.1	0.0, 0.5	Wet-Qtz
Cont. plate					70									
- Crust	32	2750	0	(50; 2 $\cdot 10^3$)	–	$1.0 \cdot 10^{-6}$	154	2.3	0.8	$1.97 \cdot 10^{17}$	1–10	0.6, 0.1	0.0, 0.05	Wet-Qtz
- Mantle	44–118		0		–	$2.2 \cdot 10^{-8}$	532	3.5	1.2	$3.98 \cdot 10^{16}$	1–10	0.6, 0.1	0.0, 0.05	Dry-Ol
Oceanic plate					70									
- Crust	20		(0.7; 0.8)		–	$2.5 \cdot 10^{-7}$	154	2.3	1.2	$1.97 \cdot 10^{17}$	1	0.1; 0.05	0.0, 0.5	Wet-Qtz
- Mantle	70		0		–	$2.2 \cdot 10^{-8}$	532	3.5	1.2	$3.98 \cdot 10^{16}$	1	0.6; 0.4	0.5, 1.5	Dry-Ol
Upper mantle	(584; 570)		0			$2.2 \cdot 10^{-8}$				$3 \cdot 10^{20}$				
Lower mantle	2340		0			$2.2 \cdot 10^{-8}$				$3 \cdot 10^{20}$; $3 \cdot 10^{23}$				
Outer core	200	10,000								$1 \cdot 10^{16}$				

drag and favours continental drift toward the trench. $\boldsymbol{F_{TD}}$ is counteracted by $\boldsymbol{F_{CD}}$ opposite in direction due to the subduction-induced mantle drag and the viscous resistance to trenchward plate drifting. The net mantle drag, $\boldsymbol{\Delta F_{MD} = F_{TD} - F_{CD}}$, when positive, pulls the continental plate against the subducting oceanic plate and determines the amount of force dissipated around the trench by (i) upper plate deformation or (ii) viscous mantle creep accommodating trench retreat. The continental strength during extensional deformation (i.e. integrated tensile strength, $\boldsymbol{B}$) is computed as follows:

$$\boldsymbol{B} = \int_0^{Y_L} \sigma_d \partial y, \tag{16}$$

where Y_L is the thickness of the lithosphere and σ_d is the maximum differential stress at each depth interval. Introducing the continental strength allows discussing the models and their comparison to nature in a more general way, which remains less dependent on the rheological parameters chosen.

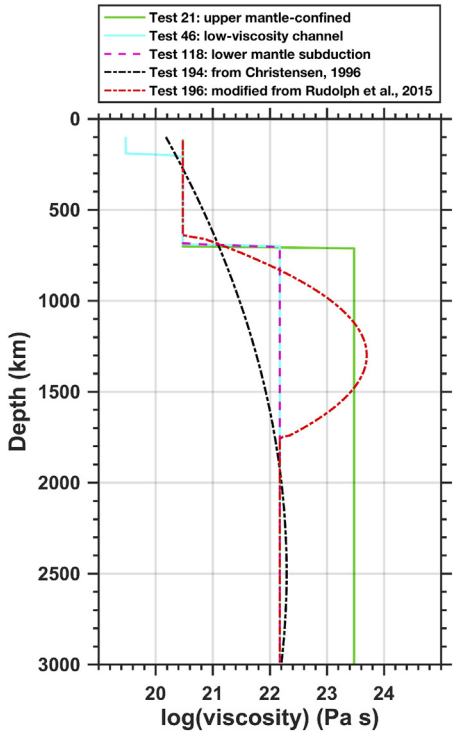

Fig. 3. Family of viscosity profiles used in this study. Test 118 and Test 21 assume a viscosity contrast from the upper to lower mantle of 50 and 1000, respectively, as proposed from joint inversion of the geoid and postglacial rebound data (e.g., Čížková et al., 2012; Mitrovica and Forte, 2004). Test 46 assumes a low viscosity channel at the asthenosphere-lithosphere boundary, as proposed by from Doglioni et al. (2011). Test 194 follows the viscosity profile suggested from Christensen (1996) and Test 196 assumes a viscosity jump in the mid-mantle as applied from Rudolph et al. (2015). Also, but not showed, a non-Newtonian upper mantle has been tested (Test 61; see Fig. 7a). For further details see Table 2.

3. Results

3.1. Upper mantle confined vs. lower mantle subduction

When the subducted oceanic lithosphere is deflected above the upper-lower mantle boundary, subduction and the induced flow remain confined to the upper mantle (Fig. 4a). From the slab-tip, the mantle moves upwards, diverging beneath the upper plate and propagating in opposite directions along the base of the lithosphere. As a result, trench-ward ($\boldsymbol{F_{TD}}$) and continent-ward ($\boldsymbol{F_{CD}}$) basal drag is generated. $\boldsymbol{F_{TD}}$ affects only a narrow portion of the continental plate not exceeding 600 km in length (Fig. 4b). This distance reflects the mantle flow cell aspect ratio of ~1, showing that the characteristic length of this process is the thickness of the convecting upper mantle $\boldsymbol{H}$, between the base of the lithosphere and the mantle transition at 660 km.

The traction-induced tension beneath the continent grows over time, as the slab sinks, inducing rifting and breakup in the back-arc. $\boldsymbol{F_{TD}}$ is complemented by trench suction ($\boldsymbol{F_{TS}}$) due to slab roll-back, pulling the continent toward the trench, and is opposed by $\boldsymbol{F_{CD}}$ due to subduction-induced mantle flow and basal viscous resistance to plate drifting acting at distances >600 km from the trench. These opposite forces generate a tension ($\boldsymbol{T}$), which is equal to the minimum of the forces between continent-ward and trench-ward plus trench suction forces: $\boldsymbol{T} = \min(|\boldsymbol{F_{CD}}|, |\boldsymbol{F_{TD}} + \boldsymbol{F_{TS}}|)$. Tension within the continent that grows along with the sinking and roll-back of the oceanic slab. When $\boldsymbol{T}$ equals the tensile strength of the continent $\boldsymbol{B}$, breakup within the upper plate occurs. In both upper-mantle confined models, the continental plate is subjected to an extensional regime, which localises at a

Table 2
Suite of the most important numerical models. The table recaps, for the most important tests, parameters such as: trenchward (F_{TD}) and continentward (F_{CD}) mantle drags, from which we defined the effective tension T = min ($|F_{TD}|$, $|F_{CD}|$) ignoring F_{TS} which is difficult to estimate; initial (B_0) and final (B_1) integrated tensile strength of the continental plate; eventual von Mises (i.e. cut-off) yield criterion as well as the age and input rheological parameters of the continental plate. The lower to upper mantle viscosity contrast (γ) (i) is not calculated for Test 061 as it changes continuously during the run due to the non-Newtonian viscosity of the upper mantle, and (ii) is set to 1 for models with a stagnant slab as no viscosity contrast exists within the convecting upper mantle.

Test	Subduction style	γ	Thickness [km]	Age [Myr]	μ_0; μ_1	Cohesion [MPa]	Von Mises [MPa]	Init-strength (B_0) [TN/m]	Final-strength (B_1) [TN/m]	Continentward drag (F_{CD}) [TN/m]	Trenchward drag (F_{TD}) [TN/m]	Tension (T) [TN/m]	Break-up
021[a]	UMC	1	76	70	0.2; 0.1	1	80	4.1	3.7	0.4	0.6	0.4	Yes
044	LMS	50	76	70	0.2; 0.1	1	300	8.8	5.3	7.5	11.7	7.5	Yes
046[b]	LMS	50	76	70	0.2; 0.1	1	300	8.8	5.3	5.1	9.5	5.1	Yes
047	LMS	150	76	70	0.2; 0.1	1	160	6.5	5.2	5.5	11.7	5.5	Yes
061[c]	LMS	/	76	70	0.2; 0.1	1	300	8.8	5.3	5.1	7.8	5.1	Yes
063	LMS	50	76	70	0.2; 0.1	1	10	0.7	0.7	3.3	1	1	Yes
086	LMS	50	150	150	0.6; 0.4	10	/	53.6	39.5	15	30.3	15.0	No
109	UMC	1	76	70	0.2; 0.1	1	10	0.7	0.7	1.5	1.1	1.1	Yes
118[a]	LMS	50	76	70	0.6; 0.6	10	/	19.9	19.9	14.6	35.3	14.6	Yes
119	LMS	50	150	150	0.2; 0.1	1	/	22.9	13.6	36.2	17.9	17.9	Yes
120	LMS	50	150	150	0.6; 0.4	1	/	53.0	38.9	35.8	23.5	23.5	No
168	LMS	50	150	150	0.6; 0.1	1	200	17.8	13.0	37.4	25.1	25.1	Yes
194	LMS	50	76	70	0.6; 0.6	10	/	19.9	19.9	15.2	34.2	15.2	Yes
196	LMS	50	76	70	0.6; 0.6	10	/	19.9	19.9	14.1	35.9	14.1	Yes

UMC: upper mantle-confined.
LMS: lower mantle subduction.
[a] Upper mantle-confined and whole mantle reference models.
[b] Model with a weak asthenospheric layer.
[c] Model with non-Newtonian upper mantle.

distance $\boldsymbol{D}$ ~ 500 km from the trench (Fig. 4a and Fig. 5a). However, since basal shearing is relatively low, breakup conditions are found only when $\boldsymbol{B} \leq 4 \cdot 10^{12}$ N/m (Fig. 5b and Table 2 – Test 021), whereas for greater strength the upper plate experiences diffused stretching. The duration of this process is <14 *Ma* and corresponds to the time taken for the slab to sink down to the transition zone. In particular, these models show that trench suction due to slab roll-back provides the breakup boundary force (estimated to be about $3–4 \cdot 10^{12}$ N/m from the difference between upper plate strength and tension generated by basal drag when breakup occurs; Test 021), while the distribution of the basal shear stress gradient ($\partial\sigma_{xy}/\partial x$) defines the location of breakup event (Fig. 4c).

When the slab penetrates deeper into the lower mantle, subduction establishes a long-term, non-steady-state evolution, with a much broader induced mantle flow (Fig. 4d). After the first stage of slab flattening above the 660 km discontinuity, deeper penetration of the oceanic lithosphere into the lower mantle may occur rapidly leading to whole mantle convection. The subduction-induced convective cell width in this case is 2900 km and has aspect ratio of ~1. This aspect ratio is a consequence of the phase transitions occurring in the pyroxene component of the pyrolitic mantle which are often ignored in mantle convection simulations, yielding much wider planforms. At high temperatures typical of upwelling mantle (>1700–1800 °C), Ringwoodite decomposes to Majorite and ferropericlase and the formation of Bridgmanite is related mostly to the Majorite ⇔ Bridgmanite transition with a positive Clapeyron slope and a large density difference (Hirose, 2002; Faccenda and Dal Zilio, 2017). This reaction occurs in the 600–750 km depth interval, generating strong positive buoyancy that favours plume penetration in the transition zone. On the other hand, within the cold slab the post-spinel and post-ilmenite reactions characterized by a negative Clapeyron slope can temporarily induce impediment to penetration. Therefore, once lower mantle subduction is attained, the combined effects of (i) downgoing slab and (ii) upwelling of hot material via subduction-induced poloidal mantle flow enhances vertical flow rather than horizontal flow with convective patterns characterized by reduced wavelengths.

This aspect ratio is similar to the upper-mantle confined subduction models, but it scales up as a consequence of deeper subduction. As the descending lithosphere lengthens, the size of the convective cell does not change, yet the slab-integrated buoyancy leads to more vigorous convection and the progressive increase of the sinking velocity $\mathbf{V_S}$ (Fig. 5b). Accordingly, the sub-continental stress profiles indicate that the basal shear stresses are much larger during lower mantle-penetrating subduction (Fig. 4e), and increase in magnitude as the slab descends. However, the planform of the mantle flow does not vary. Stress increases in two opposite directions and is equal to zero at ~3500 km from the trench for $\boldsymbol{\gamma} = 50$, corresponding to the area where mantle flow is diverging. Trench-ward shear stresses increase through time proportionally to $\mathbf{V_S}$, the slab sinking velocity, reaching an absolute shear stress peak of 17 MPa after 39 Ma. In contrast to upper-mantle confined models, the continental plate is subjected to compressional deformation around the trench as a result of the positive net mantle drag (i.e., $\boldsymbol{\Delta F_{MD}} = \boldsymbol{F_{TD}} - \boldsymbol{F_{CD}} > 0$), which pulls the upper plate against the oceanic plate. Within the plate interior, where trench suction is negligible, the basal tractions acting in opposite directions generate a force $\boldsymbol{T} = \min(|\boldsymbol{F_{CD}}|, |\boldsymbol{F_{TD}}|) = 1.46 \cdot 10^{13}$ N/m, which is high enough to break up the continental plate. For each model, breakup happens according to the maximum value of the basal shear stress gradient (Fig.

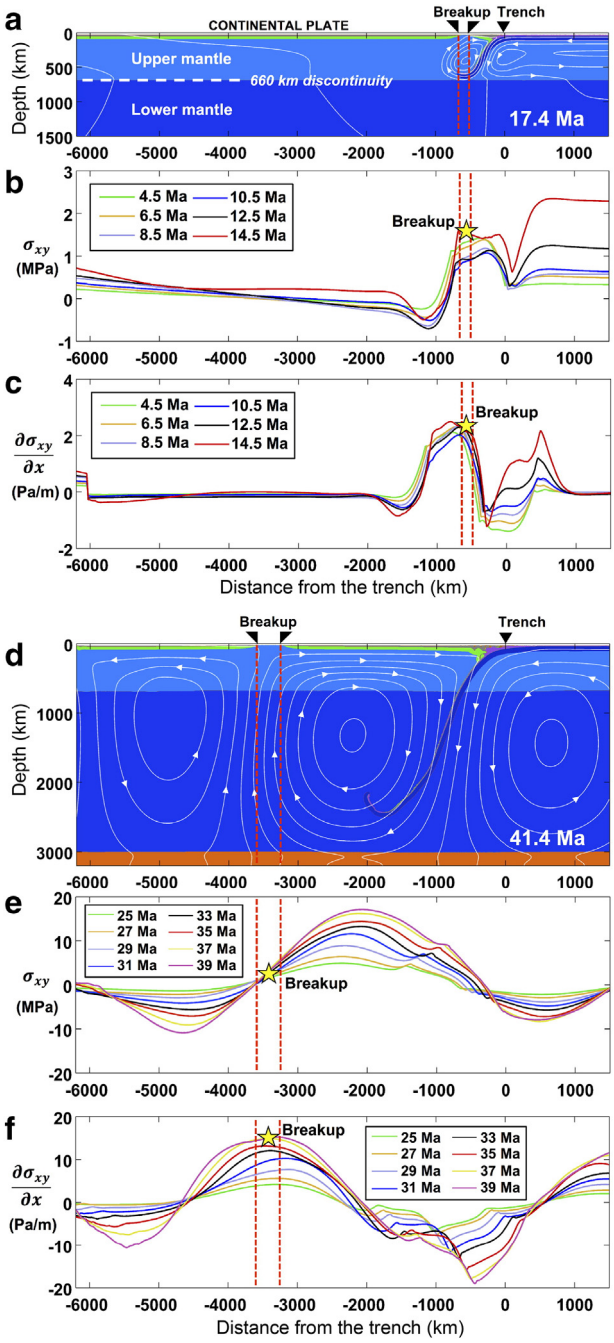

Fig. 4. Subduction-related opening of marginal and distal basins. Panels (a) and (b) show the composition field for upper-mantle confined and whole mantle reference models respectively, Table 2 - Test 021 and Test 118, with superimposed stream function at key stages of mantle-lithosphere interaction. The reference of x-axis is the trench and solid triangles delimitate the breakup region. In the top panel (a), breakup at ~500 km from the trench is the result of mantle flow induced by upper-mantle confined subduction. The breakup point shifts toward the continental interior (i.e. ranging −2850 to −3600 km from trench for a homogeneous plate depending on γ) when the slab penetrates into the lower mantle (c). Coloured curves in panels (b) and (e) show the profiles of the basal shear stress for different stages of the model in, respectively, (a) and (c). Basal shear stresses grow with time along with the slab sinking. Coloured curves in panels (b) and (f) show the profiles of the basal shear stress gradient for different stages of the model in, respectively, (a) and (c). Continental breakup localises at the peak of the shear stress gradient.

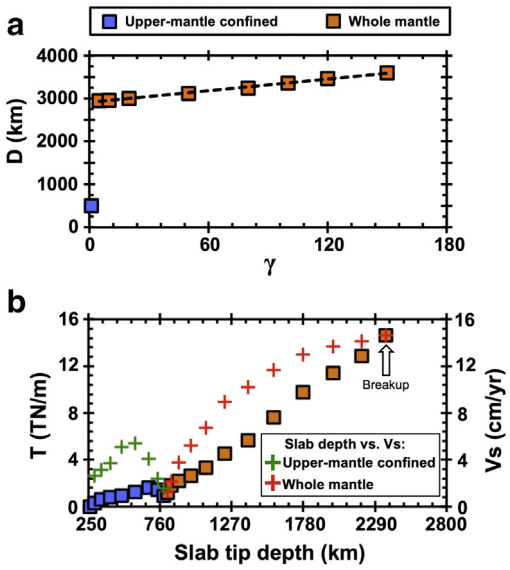

Fig. 5. (a) Distance trench-breakup $\boldsymbol{D}$ for models with constant viscosity of both upper and lower mantle and (b) Tractions $\boldsymbol{T}$ (squares) and sinking velocity $\mathbf{V_S}$ (crosses) vs. upper-lower mantle viscosity contrast $\boldsymbol{\gamma}$.

4f), where extensional stresses are maximised. Following breakup, the continent coupled with the oceanic plate drifts toward the retreating trench dragged by $\boldsymbol{F_{TD}}$, while motions of the distal continent rapidly diminish over time. At the same time, as trench-ward tractions are no longer opposed by continent-ward tractions (i.e., $\boldsymbol{F_{CD}} = 0$ and $\boldsymbol{\Delta F_{MD}} = \boldsymbol{F_{TD}}$), lithospheric thickening within the drifting plate increases significantly at the trench. For the various upper-lower mantle viscosity contrasts tested, we find that the trench–breakup distance ($\boldsymbol{D}$) is weakly dependent of the viscosity contrast, varying between ~2950 and ~3600 km for a 150–fold viscosity increase. Subducting slab penetration in the lower mantle is a longer-term process. This mantle flow configuration and the ensuing rifting regimes over ~40 Ma induce hot mantle upwelling and subsequent weakening of the upper plate. At this point in our models the continent breaks up.

A striking result of these experiments is that as we imposed a thicker and colder continent (Fig. S3), the model develops higher basal drags. As a comparison, the cratonic keel adopted in Test 168 (Table 1) develops an internal tension of ~25 TN/m in contrast to the 7.5–15 TN/m measured in experiments with a thinner upper plate. We interpret this result as an effect of the return flow that tends to be channelized within the weak upper mantle. When imposing a thicker continental plate, the upper mantle section gets thinner. As a result, upper mantle flow velocity increase raising the magnitude of mantle basal drags.

3.2. The role of continental plate heterogeneities

The presence of weak zones related to inherited structures or focused hot plumes (e.g., Gurnis, 1988; Heron et al., 2015) may favour rifting, hence constraining the breakup location. In a suite of additional models (Table 2 and Supplementary material), we have introduced a weak zone in the continental upper plate to test how this can shift the position of the rifting and the formation of distal basins (Fig. 6a). In these models, the tensile strength of the continent is $\boldsymbol{B} = 2.19 \cdot 10^{13}$ N/m, whereas in the 40 km wide weak zone the strength is reduced to $\boldsymbol{B} = 3.1 \cdot 10^{12}$ N/m. The location of this weak zone has been systematically tested at 2000 km, 4000 km and 5500 km from the trench. During the evolution of subduction in the model, relevant stresses are propagated to the weak zone through the mantle tractions. In the model where the weak zone is at a distance of 2000 km from the trench (Fig. 6b), mantle tractions remain negligible during the upper-mantle confined sinking of the slab. Tractions become relevant when the slab penetrates deeper into the lower mantle. However, since the weak zone is located above an area under compressional stresses, the strain regime is neutral and the weak zone does not deform

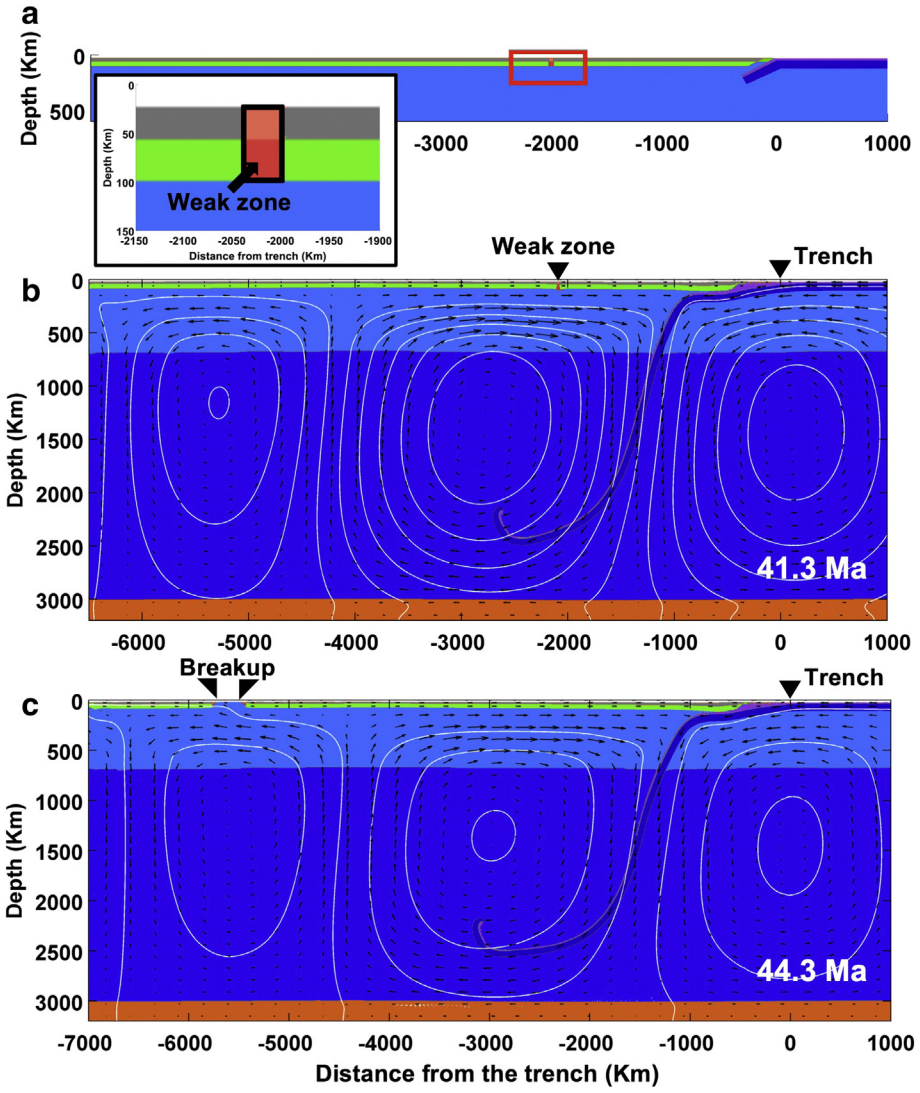

Fig. 6. Whole mantle subduction models with a continental plate with pre-existing weak zone. (a) Initial setup. The tensile strength of the continent is $\boldsymbol{B} = 2.19 \cdot 10^{13}$ N/m. The weak zone ($\boldsymbol{B} = 3.1 \cdot 10^{12}$ N/m) is 40 km wide, and is initially placed at −2000 km (b) and −5500 km (c) from the trench. Breakup occurs only when the weak zone is beyond the point where the mantle is diverging. The velocity field and the stream function are superimposed on the compositional maps.

substantially. Hence, rifting does not occur at the weak zone, but instead begins at distance $\boldsymbol{D} \approx \boldsymbol{H}$, as in the homogenous continent illustrated in the previous section. On the other hand, in the models where the weak zone is located at 4000 or at 5500 km from the trench, their position is located above (4000 km) or further than the diverging mantle tractions (5500 km) when the slab has sunk in the lower mantle (Fig. 6c). In this last case the weak zone shifts the breakup location to ~2000 km with respect to the reference model with homogeneous lithosphere. In these models breakup occurs because the weak zone is located above an area where gradients in continent-ward tractions are large (Fig. 4f). Such large gradients are found at distances $\pm \boldsymbol{D} / 2$ (half the width of the poloidal cell), implying that weak zones can shift the breakup location of 1500–2000 km. This argument is further supported by similar models of upper-mantle confined subduction, where the same process occurs and shifts in the back-arc spreading varies by ~250 km, ~$\boldsymbol{D} / 2$ (Fig. S5). In the instance of homogeneous continental lithosphere, breakup localises at a distance $\boldsymbol{D}$ ~ 500 km from the trench (Fig. 4a), which seems to be slightly larger than what we observe in back-arc basins worldwide (Currie and Hyndman, 2006). However, rheological heterogeneities may reduce the breakup distance down to ~250 km from the trench (Fig. S5). For a progressively deepening slab and propagating tractions, the heterogeneity close to the trench localises earlier, thus reducing both the minimum breakup distance to the trench and the time of rifting initiation.

3.3. The role of mantle rheology

A suite of numerical models with different rheological laws and mantle viscosity profiles demonstrate that the mechanism of breakup and drifting proposed is independent of mantle rheology. On the other hand, these different rheological properties control the breakup-trench distance ($\boldsymbol{D}$), which result in a wide range spanning from 2950 to 3650 for models with constant viscosity of both upper and lower mantle (Fig. 5a), and up to 4000 km for models with non-linear rheology (Fig. 7a). Note that, in the case of upper-mantle confined subduction, the viscosity contrast ($\boldsymbol{\gamma}$) is assumed equal to 1 (Fig. 5a), since the slab does not penetrate into the lower mantle and the upper mantle is therefore the only layer of the mantle involved. We first present a non-Newtonian upper mantle model (Fig. 7a, Table 2 – Test 061) to illustrate that similar dynamics occur for a deep sinking slab dipping gently and a wider convective cell with aspect ratio of 1.37. Thus, mantle flow diverges at a greater distance from the trench and breakup occurs at $\boldsymbol{D}$ ~ 4000 km from the trench (Fig. 7a). The viscosity within the non-Newtonian upper mantle is lower than in other models, which result in slightly

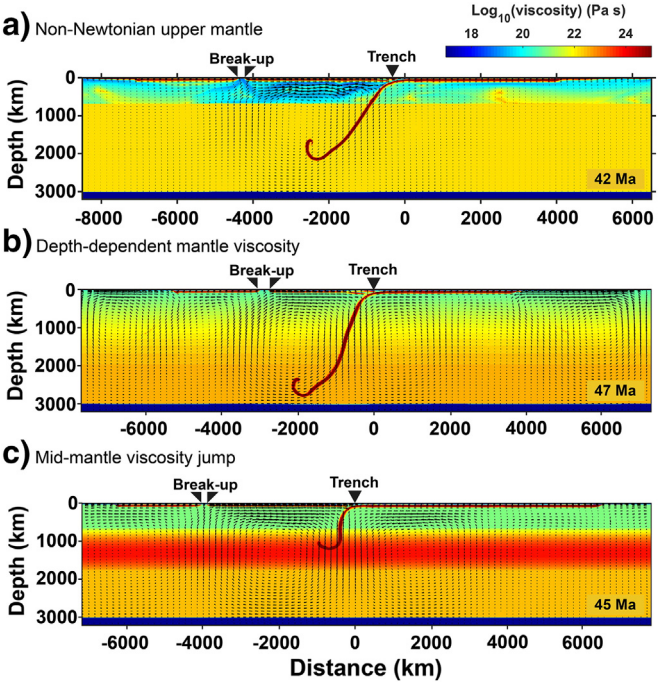

Fig. 7. Suite of three different models showing the viscosity with superimposed the velocity field (black vectors). Panel a shows the whole mantle subduction model with a non-Newtonian upper mantle (Test 61). With respect to the reference model (i.e., Test 118), the slab is more gently dipping, which induces a wider convective cell with aspect ratio of ~1.3. Thus, mantle flow diverges at a greater distance from the trench and breakup occurs at >4000 km from the trench. Corresponding data of this model are reported on Table 2 – Test 061. Panel b displays the key stage of breakup assuming a depth dependent mantle viscosity (Christensen, 1996), which results in a trench-breakup distance of ~2860 km (Test 194). Panel c shows the snapshot assuming a mid-mantle viscosity jump (e.g., Rudolph et al., 2015), which results in larger flow and thus triggering a breakup ~ 3990 km from the trench (Test 196).

lower tractions yielding a tension of $5.1 \cdot 10^{12}$ N/m. Then models with depth-dependent viscosity profiles are implemented by enforcing pressure and temperature in non-linear dependencies (Table 2) according Christensen (1996). These models result in depth-dependent increases in viscosity or, alternatively, assume a viscosity jump in the mid-mantle, as proposed by Rudolph et al. (2015) (Fig. 3). In all these models subduction displays similar characteristics, with varying degrees of interaction with the lower mantle (Fig. 7b, c). Convective cell ratios vary from 0.98–1.37 and rifting formation at large distance varies from $\boldsymbol{D}$ = 2860 km in the Test 194 (Fig. 7b) to $\boldsymbol{D}$ = 3990 km in the Test 196 (Fig. 7c).

Although we tested several different rheological profiles—which have shown to affect the shear basal drag due to a viscosity dependence on stress/strain rate—our results indicate that the planform of the mantle flow does not depend on the rheology. Despite the variations in convective cell aspect ratio, the breakup mechanism and its characteristic length are independent of the mantle rheology chosen.

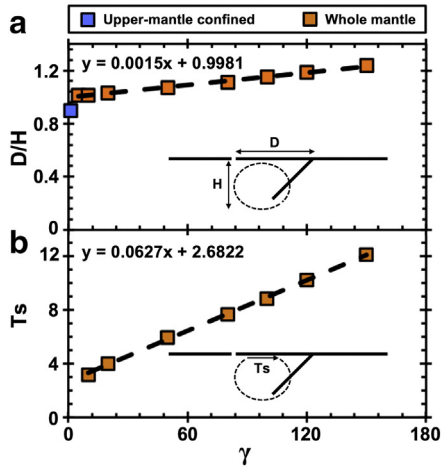

Fig. 8. Panel a shows the linear relation between $\boldsymbol{\gamma}$ and the trench-rifted margin distance ($\boldsymbol{D}$) scaled by the thickness of the convective cell ($\boldsymbol{H}$), while panel b compares $\boldsymbol{\gamma}$ and the scaled tension $\boldsymbol{T_S} = \boldsymbol{T} / (\mathbf{V_S} \cdot \boldsymbol{\eta_{UM}})$.

3.4. Similarities between back-arc and distal margin formation

In this section we illustrate the characteristics of the flow patterns arising from oceanic plate subduction, showing the scaling relationships of the breakup-trench distance ($\boldsymbol{D}$) and the basal tractions ($\boldsymbol{T}$). In the case of lower mantle subduction, the width to depth ratio ($\boldsymbol{D}/\boldsymbol{H}$) of the poloidal mantle flow is comparable to the upper-mantle confined subduction, since a $\boldsymbol{D}/\boldsymbol{H}$ value close to 1 has been found for all models. Specifically, for the different viscosity contrasts tested, this varies between 1.01 and 1.23 for increasing viscosity contrast $\boldsymbol{\gamma}$ between 5 and 150 (Fig. 8a). This illustrates that 1) the process remains similar, 2) it scales with the depth of convection $\boldsymbol{H}$, and 3) it is weakly dependent of $\boldsymbol{\gamma}$. Additionally, we illustrate that the first-order process of breakup and drifting induced by subduction is independent of mantle viscosity, although it does impact the transmitted tractions. To elucidate this last point we scale the tension as $\boldsymbol{T_S} = \boldsymbol{T} / (\mathbf{V_S} \cdot \boldsymbol{\eta_{UM}})$ (Fig. 8b) to demonstrate how and to what extent the lower mantle viscosity affects the magnitude of transmitted stresses at the base of the continental plate. By estimating the slab sinking velocity and upper/lower mantle viscosities, the development of $\boldsymbol{Ts}$ within the continent can be evaluated. It is worth noting that, as the magnitude of $\boldsymbol{T}$ increases proportionally with $\mathbf{V_S}$, the tension force induced by basal shearing is higher when slabs arrive at mid-mantle depths (Fig. 5b). The models illustrate that upper-mantle confined and whole mantle subduction provide the same conditions for breakup and drifting mechanisms, but display different lengths, durations and magnitudes. The upper-mantle confined subduction induces tractions of ~2 MPa and localises extension at distances comparable to the upper mantle thickness (~500 km). This may be shifted by 250 km due to heterogeneities, maximised at ~10 Ma from the onset of subduction. As subduction reaches the lower mantle, extension localization switches rapidly to ~3000–4000 km from the trench. This can increase to ~5000 km in the presence of continental heterogeneities. The long-term sinking of slabs in the lower mantle allows for stationary localised divergent tractions for ~40 Ma, while traction magnitude increases progressively with slab sinking up to ~18 MPa. Integrated basal shear leads to tectonic rifting forces that increase by up to ~3 times when lower mantle subduction occurs.

4. Discussion

These results shed light on the correlation between large-scale mantle flow pattern – developed during lithospheric subduction – and dynamics of continental breakup, and lead to several interesting implications. We first discuss the differences and the physical mechanism responsible for the control of subduction-induced mantle flow on the opening of both marginal and distal basins, evaluating for which continental strengths breakup may occur. Subsequently, we make a comparison between the natural cases and our numerical experiments. Finally, we discuss involved modeling limitations.

4.1. Comparing opening of marginal vs. distal basins

With the support of numerical models, we have illustrated the similarities between rifting mechanisms that act within continental upper plates above subduction. The modeling suggests that marginal back-

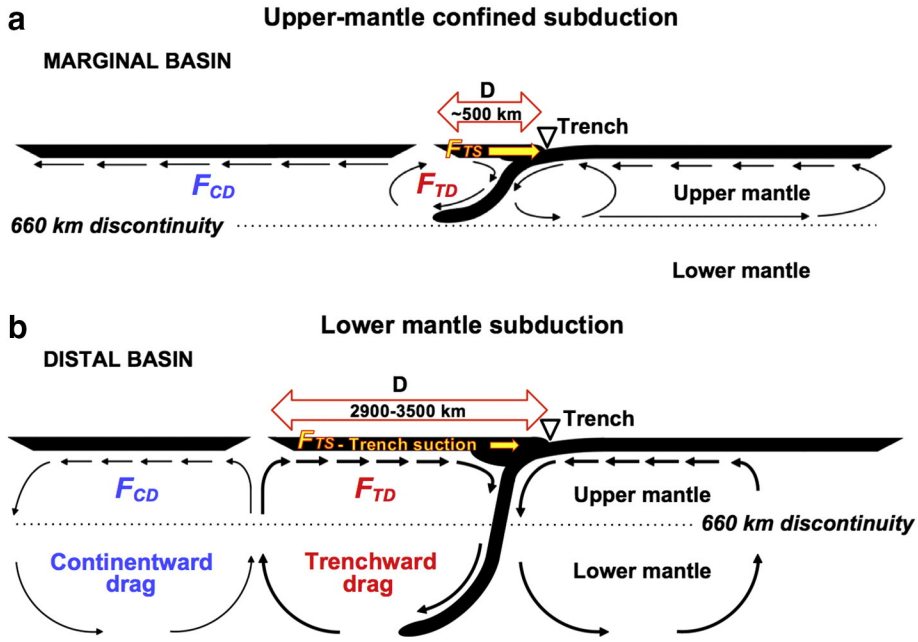

Fig. 9. Synoptic view of the subduction-induced mantle flow and continental breakup. Panel (a) and (b) are for the upper-mantle confined and whole mantle subduction models, respectively. Thicker black arrows indicate more vigorous mantle flow and basal tractions. Trench suction forces (yellow arrow) act within the upper plate in proximity of the trench and are stronger in upper-mantle confined subduction models. In whole mantle subduction models the continental plate is subjected to compressional deformation and lithospheric thickening near the trench. Distances of (a) marginal and of (b) distal basins from the trench are those found in models with a homogeneous continent.

arc basins and distal basins respond to the same mechanism: trenchward tractions generated by return flow associated with subduction. The localised rifting within continental plates is correspondingly controlled by the depth of convection (Fig. 9). Whereas in upper-mantle confined subduction the characteristic distance is comparable to the upper mantle thickness (Fig. 9a), for lower mantle subduction the distance becomes comparable to the whole mantle (Fig. 9b). With large-scale return flow beneath the supercontinent, extensional stresses localise thousands of kilometres from the trench, but compression remains localised near the trench. This feature is well defined in lower mantle subduction down to a depth of >1000 km, and similar results have recently been obtained by Yang et al. (2016) and Faccenna et al. (2017) with application to South-East Asia and the Andes, respectively. Further sinking of subducting slabs in the deep mantle, while maintaining the same planform of the mantle flow, increases the velocity of poloidal flow and, in turn, the shear stresses transmitted at the base of the continent. Because subduction and mantle convection flow cells comprise only two possible modalities, a bimodal distribution of basin-trench distances is predicted. This bimodal distribution is depicted in Fig. 10, which shows the comparison between trench-break distance (***D***) and the tensile strength (***B***) of continents from models exhibiting continental breakup. Note that the two regions highlighted in grey, ranging from 10^{12} to 10^{14} N/m, define the spectrum of natural continental strengths based on a global compilation framework (Burov, 2010). Plotted results are from the suite of models with homogenous and heterogeneous continents, as well as from numerical experiments with a non-Newtonian upper mantle rheology. It can be observed that the model predictions are in good agreement with the observed distribution of trench-to-rifted margin distances (Fig. 10). Available back-arc distance measurements (e.g., Currie and Hyndman, 2006) show that the minimum distance of trench-back arc rifting on Earth varies between ~250 to ~400 km. These values are compatible with the rifting distance in our model, given pristine continent and pre-existing heterogeneities.

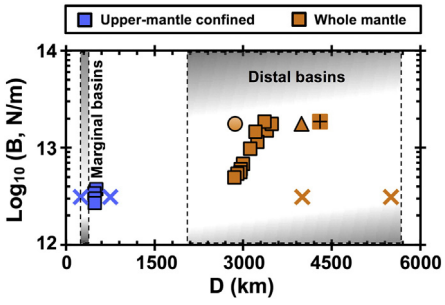

Fig. 10. Comparisons of ***D*** and ***B*** of models exhibiting continental breakup with observations on Earth. The range of natural ***B*** (Burov, 2010) and ***D*** for marginal and distal basins (see Supplementary Table S1) define two regions highlighted in grey, within which most numerical results fall. Plotted results are for models with: homogenous continent and upper mantle with constant viscosity (squares), homogenous continent and non-Newtonian upper mantle (square with cross), and heterogeneous continent with a weak zone at various distances from the trench (crosses).

4.2. Possible applications to natural examples

The two continental breakup end-members can potentially be applied to many natural examples where geological and geophysical data support our numerical experiments. For instance, the mechanism for marginal basin formation is in agreement with the reconstructed Mediterranean evolution (Jolivet and Faccenna, 2000), Cenozoic Pacific subduction and evolution of the Sea of Japan (Miller and Kennett, 2006), as well as other published modeling results (e.g., Capitanio et al., 2010; Gerya and Meilick, 2011; Gurnis et al., 2004). In the Western Mediterranean, the Liguro-Provençal back-arc basin opened at a distance of ~400 km from the migrating convergent margin (Carminati et al., 2012), while the Ligurian lithosphere was subducted down to the transition zone (Faccenna et al., 2001; Piromallo and Morelli, 2003). Our upper-mantle confined models indicate that the upper plate yields only under specific conditions dictated by the continental strength (see Table 2). When this latter is too strong, the continental plate could undergo long-term stretching without breakup. This might be the case of the Eastern Mediterranean, where the incipient Aegean back-arc basin, located further north of the Rhodope massive, by 65–

50 Ma (Jolivet and Brun, 2010), is placed ~400–450 km from the convergent margin, and is followed by the progressive migration of amagmatic exhumation events of metamorphic core complexes (e.g., Jolivet et al., 2013) and no break-up, in agreement with an initially thickened lithosphere. The extensional centres have constantly migrated along with the convergent margin, keeping a similar distance of ~400 km. In the case of Japan Sea, instead, the continental breakup occurred at smaller distance, likely 270–350 km from the trench, and was followed by the migration of the narrow Japan arc through an initial amagmatic event (Jolivet et al., 1994). The evolution of the Sea of Japan is compatible with reconstructions of the down-going Pacific lithosphere (e.g., Fukao et al., 2009), which indicate slab subduction, retreat and stagnation over the transition zone. Although the distance is here smaller, it is still compatible with the effect of pre-existing weaknesses, reducing the break-up location to similar distance. Besides inherited weak structures, other processes not taken into account in our models such as lithospheric mantle metasomatization via slab dehydration and arc-magmatism could weaken lithospheric portions much closer (100–250 km) to the trench than predicted by our homogeneous upper plate models.

Following the same line of reasoning, we propose that a similar mechanism assisted the rifting and breakup of Western Pangea, and the opening of the Atlantic Ocean. We have measured the range of trench-to-rift distances (Supplementary Fig. S7 and Table S1) between the current American trenches and the Atlantic Ocean continental margin, which vary between 2000 and 5000 km. These distances can be explained by our simplified 2D models, when heterogeneities in the lithosphere are accounted for. According to the mechanism illustrated here, the localisation of long-term extensional regimes at large distances from the trench is compatible with deep lithosphere subduction and induced large-scale mantle flow. Taking into account the seismic structure of the mantle and plate motions, the inverse mantle convection model proposed in (Liu et al., 2008) shows the evolution of deep Farallon subduction is characterized by a large-scale, vigorous, and long-lasting mantle flow pattern. This regime is in accordance with the model proposed here. Therefore, large-scale flow due to deep subduction may have led to a long-lived extensional regime during the rifting of Western Pangea and subsequent opening of the Atlantic. The range of trench to rifted margin distances (2000–5000 km) can be explained by either inherited weak structures (e.g., Buiter and Torsvik, 2014) or thermal weakening due to impinging plumes. These plumes may have affected the position of continental breakup, although they are not necessarily required for our models. While the location of the rifting is only mildly affected by heterogeneities in the continent, the exact timing of the rifting depends on this and the deeper subduction. Although the overall strength of the Pangea continent cannot be constrained, our modeling illustrates that relevant basal tensile forces might have overcome its strength only when the subducting slab reached the deep lower mantle. Reconstructed deep mantle slab subduction suggests this occurred prior to 100 Ma (Lithgow-Bertelloni and Richards, 1998), corresponding to the initial opening of the Atlantic Ocean (~130 Ma; Seton et al., 2012). Large-scale flow due to deep subduction and related basal drag has also been invoked by Husson et al. (2012) to explain the westward drift of South America, although the break-up event has been related only to active upwellings beneath Africa rather than to sustained basal tractions.

Subduction-induced basal tractions could have similarly contributed to the dismembering of the Eastern Pangea continent during the Late Jurassic-Cretaceous period Mesozoic, when the Phoenix plate subducted beneath Antarctica and East Gondwana at distances from the rifting continental margin which are consistent with the 2000–5000 km found in our experiments (Seton et al., 2012).

Intra-continental breakup in response to deep subduction would not be effective when basal tractions are unable to overcome the upper plate lithospheric strength. This would explain why Eurasia did not break-up during the Mesozoic-Early Cenozoic deep subduction of the Tethyan slab below its southern margin (Seton et al., 2012). Indeed, seismic tomography models indicate that large portions of Eurasia have characteristic thick cratonic roots, except toward the continent eastern margins (Schaeffer and Lebedev, 2013; Chang et al., 2015) where lithospheric thinning likely occurred during Mesozoic-Cenozoic tectonic processes (Griffin et al., 1998).

4.3. Modeling limitations

The main limitation of our simulations is represented by their two-dimensional nature, which does not allow analysing the role of transtensional/transpressional deformation, lateral extrusion nor toroidal mantle flow. Furthermore, in a 3D convective mantle characterized by several subducting slabs and upwelling plumes, the mantle flow patterns are likely different when those generated in our 2D models by a single subducting plate. However, two- and three-dimensional convection models and several pieces of geological data indicate that, consistent with our results, mantle upwellings primarily occur in response to subduction and at distances from the trench comparable to the whole mantle thickness (e.g., Heron et al., 2015). Furthermore, despite the absence of toroidal flow, which has been shown to be relevant in 3D models of subduction (e.g., Stegman et al., 2010), basal tractions due to poloidal mantle return flow are large enough to generate significant extensional stresses in our 2D models, and find accordance with previous works (e.g., Holt et al., 2015). It follows that, although simplified, the present analysis is applicable to real subduction-breakup systems, providing a first-order estimate of the subduction-related tensional forces generated within the continent.

It is also important to stress that continent breakup solely due to the impingement of actively upwelling plumes has only been observed in two-dimensional numerical models (e.g., Gurnis, 1988). This is because a 2D plume generates a diverging mantle flow similar to that induced by subducting slabs, which is equivalent to assuming that vertical walls of upwelling buoyant material are present within the Earth's mantle. However, in a real 3D environment low-viscosity mantle plumes are columnar features (e.g., French and Romanowicz, 2015; van Keken, 1997) and induce axi-symmetric mantle flow and ridge-push forces that do not trigger continental breakup, but help in localising the far-field tensional stresses (Burov and Gerya, 2014). Axi-symmetric mantle flow could potentially trigger rifting or breakup without far-field tensional stresses when the continent displays mechanical anisotropy or is free to deform only along certain directions, but it is unclear whether full oceanization of the margin could be achieved and 3D numerical studies are envisaged in order to test this hypothesis. On the other hand, subduction-induced poloidal mantle flow can be considered two-dimensional for sufficiently large plates, striking along the trench for hundreds or thousands of km and, as shown by numerical results, generating the required far-field tensional forces able to breakup a large continental plate. The geological and geophysical data suggest that Pangea has been mostly bounded by long-term and deep subduction zones, which support our idea that the sustained basal tractions likely played a fundamental role for the dismembering of the supercontinent.

5. Conclusions

Numerical modeling is used to investigate the independent role of subduction and induced mantle flow in the rifting and breakup of continental upper plates. We illustrate that, as subducting slabs sink in the upper mantle, the counter flow of the mantle localises diverging tractions at the base of the upper plate, which may undergo rifting in the back-arc, forming marginal basins. The process is similar when the slabs sink deeper in the lower mantle. Here, however, the perturbation of the lower mantle upon subduction reorganises the flow in much larger convective cells. In this case, extensional tractions are propagated for much greater distances within continent interiors. Because size, wavelength and shape of convective cells in the mantle do not vary

with depth of subduction, the location of the diverging flow is a stable feature, only mildly affected by the rheological regime of the mantle (non-Newtonian, temperature-pressure dependent, upper to lower mantle viscosity contrast). Although the convective cell reorganises rapidly upon lower mantle penetration, tractions increase progressively with depth of subduction as a consequence of larger slab mass, subduction velocity, and flow velocity.

In quantifying the basal forces exerted by subduction-induced mantle flow beneath continental plates, tractions in the order of ~0.5–1.5 $\cdot 10^{12}$ N/m are propagated to upper plates when subduction is confined to the upper mantle. These increase by >10 times when the slabs are in the lower mantle. The consequence of such tractions is that upper plates rift and eventually breakup. This occurs in the same location as the underlying diverging flow, which is ~500 km above upper-mantle confined subductions and where marginal basins form. In the latter case, rifting is aided by trench-suction forces that are effective near the trench and complement basal drag. While pre-existing weaknesses can shift the rifting location, they are effective only when located directly above areas characterized by strong gradients in basal tractions (~250 km for marginal basins and ~2000 km for distal basins).

These processes have distinct durations: while breakup occurs within <10 Ma when subduction is confined in the upper mantle, a tensile regime can be sustained for ~40 Ma before breakup when subduction penetrates deeper. Subduction through the lower mantle could be hampered by compositional variations acting to reduce the slab negative buoyancy and thus its sinking velocity (e.g., Ballmer et al., 2015). In this case, the sustained tensile regime would act for longer time intervals albeit with lower traction magnitudes. Additionally, the duration may be altered by pre-existing weaknesses and diverse lithospheric strength, although any quantification is speculative. By inference, the timing of breakup is probably more relevant during lower mantle penetration, which is required to produce tractional forces comparable to the strength of strong cratons.

When compared to observations, our models reproduce the range of both marginal and distal basins. While the mechanisms for the formation of marginal basins are known, our results support the idea that the same mechanism, although scaled up, is at work beneath large continents. Although other mechanisms play relevant roles, deep subduction is clearly a major factor in the deformation of plate interiors and the ensuing breakup of supercontinents. Hence, the breakup and dispersal of continents operates through the same broad dynamic as that driving their aggregation.

Acknowledgements

This work was completed as part of the MSc thesis of Luca Dal Zilio and was supported by Progetto di Ateneo FACCPRAT2012 granted by Università degli Studi di Padova to Manuele Faccenda. Numerical simulations were performed on the CINECA cluster (Bologna, Italy). We thank Taras Gerya, Paul Tackley and Gabriele Morra for fruitful discussions and comments, and Suzanne Atkins for improving the English of the manuscript. This manuscript benefited from the comments of Claudio Faccenna and an anonymous reviewer as well as from suggestions by editors Philippe Agard and Fernando Ornelas Marques.

Appendix A. Supplementary data

Supplementary data to this article can be found online at http://dx.doi.org/10.1016/j.tecto.2017.03.006.

References

Ballmer, M.D., Schmerr, N.C., Nakagawa, T., Ritsema, J., 2015. Compositional mantle layering revealed by slab stagnation at ~1000-km depth. Sci. Adv. 1 (11).
Běhounková, Marie, Čížková, Hana, 2008. Long-wavelength character of subducted slabs in the lower mantle. Earth Planet. Sci. Lett. 275 (1), 43–53.
Bercovici, David, Long, Maureen D., 2014. Slab rollback instability and supercontinent dispersal. Geophys. Res. Lett. 41 (19), 6659–6666.
Buiter, Susanne J.H., Torsvik, Trond H., 2014. A review of Wilson Cycle plate margins: a role for mantle plumes in continental break-up along sutures? Gondwana Res. 26 (2), 627–653.
Bunge, Hans-Peter, Richards, Mark A., Lithgow-Bertelloni, Carolina, Baumgardner, John R., Grand, Stephen P., Romanowicz, Barbara A., 1998. Time scales and heterogeneous structure in geodynamic Earth models. Science 280 (5360), 91–95.
Burov, Evgueni, 2010. Plate rheology and mechanics. Crust and Lithosphere Dynamics: Treatise on Geophysics 6, 99.
Burov, Evgueni, Gerya, Taras, 2014. Asymmetric three-dimensional topography over mantle plumes. Nature 513 (7516), 85–89.
Capitanio, Fabio, Stegman, Dave, Moresi, Louis-Noel, Sharples, Wendy, 2010. Upper plate controls on deep subduction, trench migrations and deformations at convergent margins. Tectonophysics 483 (1), 80–92.
Carminati, Eugenio, Lustrino, Michele, Doglioni, Carlo, 2012. Geodynamic evolution of the central and western Mediterranean: tectonics vs. igneous petrology constraints. Tectonophysics 579, 173–192.
Chang, S.-J., Ferreira, A.M.G., Ritsema, J., van Heijst, H.J., Woodhouse, J.H., 2015. Joint inversion fro global isotropic and radially anisotropic mantle structure including crustal thickness perturbations. J. Geophys. Res. 120, 4278–4300.
Christensen, Ulrich R., 1996. The influence of trench migration on slab penetration into the lower mantle. Earth Planet. Sci. Lett. 140 (1), 27–39.
Čížková, Hana, van den Berg, Arie P., Spakman, Wim, Matyska, Ctirad, 2012. The viscosity of Earth's lower mantle inferred from sinking speed of subducted lithosphere. Phys. Earth Planet. Inter. 200, 56–62.
Connolly, James A.D., 2005. Computation of phase equilibria by linear programming: a tool for geodynamic modeling and its application to subduction zone decarbonation. Earth Planet. Sci. Lett. 236 (1), 524–541.
Currie, Claire A., Hyndman, Roy D., 2006. The thermal structure of subduction zone back arcs. J. Geophys. Res. Solid Earth 111 (B8).
Doglioni, Carlo, Ismail-Zadeh, Alik, Panza, Giuliano, Riguzzi, Federica, 2011. Lithosphere–asthenosphere viscosity contrast and decoupling. Phys. Earth Planet. Inter. 189 (1), 1–8.
Faccenda, Manuele, Dal Zilio, Luca, 2017. The role of solid–solid phase transitions in mantle convection. Lithos 268, 198–224.
Faccenna, Claudio, Becker, Thorsten W., Lucente, Francesco Pio, Jolivet, Laurent, Rossetti, Federico, 2001. History of subduction and back arc extension in the Central Mediterranean. Geophys. J. Int. 145 (3), 809–820.
Faccenna, C., Becker, T.W., Lallemand, S., Lagabrielle, Y., Funiciello, F., Piromallo, C., 2010. Subduction-triggered magmatic pulses: a new class of plumes? Earth Planet. Sci. Lett. 299 (1), 54–68.
Faccenna, C., Oncken, O., Holt, A.F., Becker, T.W., 2017. Initiation of the Andean orogeny by lower mantle subduction. Earth Planet. Sci. Lett. 463, 189–201.
French, Scott W., Romanowicz, Barbara, 2015. Broad plumes rooted at the base of the Earth's mantle beneath major hotspots. Nature 525 (7567), 95–99.
Fukao, Yoshio, Obayashi, Masayuki, Nakakuki, Tomoeki, 2009. Stagnant slab: a review. Annu. Rev. Earth Planet. Sci. 37, 19–46.
Garel, Fanny, Goes, Saskia, Davies, D.R., Davies, John Huw, Kramer, Stephan C., Wilson, Cian R., 2014. Interaction of subducted slabs with the mantle transition-zone: a regime diagram from 2-D thermo-mechanical models with a mobile trench and an overriding plate. Geochem. Geophys. Geosyst. 15 (5), 1739–1765.
Garfunkel, Z., Anderson, C.A., Schubert, G., 1986. Mantle circulation and the lateral migration of subducted slabs. J. Geophys. Res. 91, 7205–7223.
Gerya, Taras, 2010. Introduction to Numerical Geodynamic Modelling. Cambridge University Press.
Gerya, T.V., Meilick, F.I., 2011. Geodynamic regimes of subduction under an active margin: effects of rheological weakening by fluids and melts. J. Metamorph. Geol. 29 (1), 7–31.
Gerya, Taras V., Yuen, David A., 2003. Characteristics-based marker-in-cell method with conservative finite-differences schemes for modeling geological flows with strongly variable transport properties. Phys. Earth Planet. Inter. 140 (4), 293–318.
Gerya, Taras V., Connolly, James A.D., Yuen, David A., 2008. Why is terrestrial subduction one-sided? Geology 36 (1), 43–46.
Griffin, W.L., Zhang, A.D., O'Reilly, S.Y., Ryan, C.G., 1998. Phanerozoic evolution of the lithosphere beneath the Sino-Korean craton. In: Flower, M.F.J., et al. (Eds.), Mantle Dynamics and Plate Interaction in East Asia. Geodyn. Ser. 27. Am. Geophy. Union, Washington, D.C., pp. 107–126.
Gurnis, Michael, 1988. Large-scale mantle convection and the aggregation and dispersal of super- continents. Nature 332 (6166), 695–699.
Gurnis, Michael, Hall, Chad, Lavier, Luc, 2004. Evolving force balance during incipient subduction. Geochem. Geophys. Geosyst. 5 (7).
Heron, Philip J., Lowman, Julian P., 2011. The effects of supercontinent size and thermal insulation on the formation of mantle plumes. Tectonophysics 510 (1), 28–38.
Heron, Philip J., Lowman, Julian P., Stein, Claudia, 2015. Influences on the positioning of mantle plumes following supercontinent formation. J. Geophys. Res. Solid Earth 120 (5), 3628–3648.
Hirose, K., 2002. Phase transitions in pyrolitic mantle around 670-km depth: implications for upwelling of plumes from the lower mantle. J. Geophys. Res. Solid Earth 107 (B4).
Holt, A.F., Becker, T.W., Buffett, B.A., 2015. Trench migration and overriding plate stress in dynamic subduction models. Geophys. J. Int. 201 (1), 172–192.
Husson, L., Conrad, C.P., Faccenna, C., 2012. Plate motions, Andean orogeny, and volcanism above the South Atlantic convection cell. Earth Planet. Sci. Lett. 317-318, 126–135.
Jolivet, L., Brun, J.P., 2010. Cenozoic geodynamic evolution of the Aegean. Int. J. Earth Sci. 99 (1), 109–138.
Jolivet, L., Faccenna, C., 2000. Mediterranean extension and the Africa-Eurasia collision. Tectonics 19 (6), 1095–1106.

Jolivet, Laurent, Tamaki, Kensaku, Fournier, Marc, 1994. Japan Sea, opening history and mechanism: a synthesis. Journal of Geophysical Research: Solid Earth (1978–2012) 99 (B11), 22237–22259.
Jolivet, Laurent, Faccenna, Claudio, Huet, Benjamin, Labrousse, Loïc, Le Pourhiet, Laetitia, Lacombe, Olivier, Lecomte, Emmanuel, Burov, Evgueni, Denele, Yoann, Brun, Jean-Pierre, et al. 2013. Aegean tectonics: strain localisation, slab tearing and trench retreat. Tectonophysics, 597, 1–33.
Katayama, Ikuo, Karato, Shun-ichiro, 2008. Low-temperature, high-stress deformation of olivine under water-saturated conditions. Phys. Earth Planet. Inter. 168 (3), 125–133.
van Keken, Peter, 1997. Evolution of starting mantle plumes: a comparison between numerical and laboratory models. Earth Planet. Sci. Lett. 148 (1), 1–11.
King, Scott D., Frost, Daniel J., Rubie, David C., 2015. Why cold slabs stagnate in the transition zone. Geology 43 (3), 231–234.
Koptev, Alexander, Calais, Eric, Burov, Evgueni, Leroy, Sylvie, Gerya, Taras, 2015. Dual continental rift systems generated by plume-lithosphere interaction. Nat. Geosci. 8 (5), 388–392.
Lenardic, A., Richards, M.A., Busse, F.H., 2006. Depth-dependent rheology and the horizontal length scale of mantle convection. J. Geophys. Res. Solid Earth 111 (B7).
Lenardic, Adrian, Moresi, L., Jellinek, A.M., O'neill, C.J., Cooper, C.M., Lee, C.T., 2011. Continents, supercontinents, mantle thermal mixing, and mantle thermal isolation: theory, numerical simulations, and laboratory experiments. Geochem. Geophys. Geosyst. 12 (10).
Li, Chang, van der Hilst, Robert D., Engdahl, E. Robert, Burdick, Scott, 2008. A new global model for P wave speed variations in Earth's mantle. Geochem. Geophys. Geosyst. 9 (5).
Lithgow-Bertelloni, Carolina, Richards, Mark A., 1998. The dynamics of Cenozoic and Mesozoic plate motions. Rev. Geophys. 36 (1), 27–78.
Liu, Lijun, Spasojević, Sonja, Gurnis, Michael, 2008. Reconstructing Farallon plate subduction beneath North America back to the Late Cretaceous. Science 322 (5903), 934–938.
Lowman, Julian P., Jarvis, Gary T., 1996. Continental collisions in wide aspect ratio and high Rayleigh number two-dimensional mantle convection models. Journal of Geophysical Re- search: Solid Earth 101 (B11), 25485–25497.
Melosh, Jay, 1977. Shear stress on the base of a lithospheric plate. Pure Appl. Geophys. 115 (1–2), 429–439.
Miller, Meghan S., Kennett, Brian L.N., 2006. Evolution of mantle structure beneath the northwest Pacific: evidence from seismic tomography and paleogeographic reconstructions. Tectonics 25 (4).
Mitrovica, J.X., Forte, A.M., 2004. A new inference of mantle viscosity based upon joint inversion of convection and glacial isostatic adjustment data. Earth Planet. Sci. Lett. 225 (1), 177–189.
Piromallo, Claudia, Morelli, Andrea, 2003. P wave tomography of the mantle under the Alpine-Mediterranean area. Journal of Geophysical Research: Solid Earth (1978–2012) 108 (B2).
Ranalli, Giorgio, 1995. Rheology of the Earth. Springer.
Rudolph, Maxwell L., Lekić, Vedran, Lithgow-Bertelloni, Carolina, 2015. Viscosity jump in Earth's mid-mantle. Science 350 (6266), 1349–1352.
Schaeffer, A.J., Lebedev, S., 2013. Global shear speed structure of the upper mantle and transition zone. Geophys. J. Int. 194, 417–449.
Seton, M., Müller, R.D., Zahirovic, S., Gaina, C., Torsvik, T., Shephard, G., Talsma, A., Gurnis, M., Turner, M., Maus, S., et al., 2012. Global continental and ocean basin reconstructions since 200 Ma. Earth Sci. Rev. 113 (3), 212–270.
Stegman, D.R., Farrington, Rebecca, Capitanio, F.A., Schellart, W.P., 2010. A regime diagram for subduction styles from 3-D numerical models of free subduction. Tectonophysics 483 (1), 29–45.
Tackley, Paul J., Stevenson, David J., Glatzmaier, Gary A., Schubert, Gerald, 1993. Effects of an endothermic phase transition at 670 km depth in a spherical model of convection in the Earth's mantle. Nature 361 (6414), 699–704.
Tan, Eh., Gurnis, Michael, Han, Lijie, 2002. Slabs in the lower mantle and their modulation of plume formation. Geochem. Geophys. Geosyst. 3 (11), 1–24.
Wilson, J. Tuzo, 1966. Did the Atlantic close and then re-open? Nature.
Yang, T., Gurnis, M., Zahirovic, S., 2016. Mantle-induced subsidence and compression in SE Asia since the early Miocene. Geophys. Res. Lett. 43 (5), 1901–1909.
Yoshida, Masaki, 2014. Effects of various lithospheric yield stresses and different mantle-heating modes on the breakup of the Pangea supercontinent. Geophys. Res. Lett. 41 (9), 3060–3067.
Zhang, Nan, Zhong, Shijie, Leng, Wei, Li, Zheng-Xiang, 2010. A model for the evolution of the Earth's mantle structure since the Early Paleozoic. J. Geophys. Res. Solid Earth 115 (B6).
Zhao, D., 2004. Global tomographic images of mantle plumes and subducting slabs: insight into deep Earth dynamics. Phys. Earth Planet. Inter. 146 (1), 3–34.
Zhao, D., Tian, Y., Lei, J., Liu, L., Zheng, S., 2009. Seismic image and origin of the Changbai intraplate volcano in East Asia: role of big mantle wedge above the stagnant Pacific slab. Phys. Earth Planet. Inter. 173 (3), 197–206.
Zhong, Shijie, Gurnis, Michael, 1993. Dynamic feedback between a continentlike raft and thermal convection. J. Geophys. Res. Solid Earth 98 (B7), 12219–12232.
Zhong, Shijie, Liu, Xi, 2016. The long-wavelength mantle structure and dynamics and implications for large-scale tectonics and volcanism in the Phanerozoic. Gondwana Res. 29 (1), 83–104.
Zhong, Shijie, Zhang, Nan, Li, Zheng-Xiang, Roberts, James H., 2007. Supercontinent cycles, true polar wander, and very long-wavelength mantle convection. Earth Planet. Sci. Lett. 261 (3), 551–564.